












## Three-axis flexible tube sensor with LSTM-based force prediction for alignment of electric vehicle charging ports

Hendri Maja Saputra <sup>a,b,\*</sup> , Ahmad Pahrurrozi <sup>c</sup> ,  
Catur Hilman Adritya Haryo Bhakti Baskoro <sup>a</sup> , Nur Safwati Mohd Nor <sup>b</sup> ,  
Nanang Ismail <sup>c</sup> , Estiko Rijanto <sup>a</sup> , Edwar Yazid <sup>a</sup> , Mohd Zarhamdy Md Zain <sup>b</sup> ,  
Intan Zaurah Mat Darus <sup>b</sup> 

<sup>a</sup> Research Center for Smart Mechatronics, National Research and Innovation Agency (BRIN)  
Kawasan Sains dan Teknologi (KST) Samaun Samadikun, Jalan Sangkuriang, Bandung, 40135, Indonesia

<sup>b</sup> Faculty of Mechanical Engineering, University of Technology Malaysia (UTM)  
UTM Johor Bahru, Johor Darul Takzim, 81310, Malaysia

<sup>c</sup> Department of Electrical Engineering, Sunan Gunung Djati State Islamic University Bandung (UIN SGD)  
Jalan A.H. Nasution No. 105, Bandung, 40614, Indonesia

### Abstract

This paper introduces a novel three-axis flexible tube sensor designed for force measurement in electric vehicle (EV) charging port alignment, utilizing long short-term memory (LSTM) networks. The research aims to develop and validate a flexible and accurate sensor system capable of predicting multi-axis forces during alignment. The sensor integrates a magnetic sensor at the center of a flexible tube to capture three-dimensional (3-D) magnetic field variations corresponding to force changes. Fabricated using thermoplastic polyurethane (TPU) via 3-D printing technology, the sensor leverages machine learning to predict force values along the  $x$ ,  $y$ , and  $z$  axes ( $F_x$ ,  $F_y$ ,  $F_z$ ). Finite element method (FEM) analysis was conducted to assess the deflection characteristics of the flexible tube under various force conditions. Experimental results demonstrate that integrating LSTM significantly enhances the accuracy of force prediction, achieving an  $R^2$  score exceeding 97 % for all axes, with mean squared error (MSE) values of 0.2819 for the  $x$ -axis, 0.3567 for the  $y$ -axis, and 2.8086 for the  $z$ -axis. The sensor is capable of measuring forces up to 30 N without exceeding its elastic limits. These findings highlight the sensor's potential for improving alignment accuracy and reliability in automated EV charging systems.

Keywords: finite element method (FEM) analysis; flexible tube sensor; force measurement; long short-term memory (LSTM) neural network; three-axis force prediction.

### I. Introduction

Accurate force measurement is crucial in applications like electric vehicle (EV) charging port alignment [1][2]. Integrating force sensors in robotic

charging systems ensures precise plugging, preventing mechanical damage and ensuring efficient operations. Research into robotic charging, particularly manipulators, is essential. A detailed discussion of the four degree of freedom (4 DOF) prismatic-revolute-

\* Corresponding Author. [hend037@brin.go.id](mailto:hend037@brin.go.id) (H. M. Saputra)

<https://doi.org/10.55981/j.mev.2024.1104>

Received 28 November 2024; revised 13 December 2024; accepted 16 December 2024; available online 31 December 2024; published 31 December 2024

2088-6985 / 2087-3379 ©2024 The Authors. Published by BRIN Publishing. MEV is Scopus indexed Journal and accredited as Sinta 1 Journal. This is an open access article CC BY-NC-SA license (<https://creativecommons.org/licenses/by-nc-sa/4.0/>).

How to Cite: H. M. Saputra *et al.*, "Three-axis flexible tube sensor with LSTM-based force prediction for alignment of electric vehicle charging ports," *Journal of Mechatronics, Electrical Power, and Vehicular Technology*, vol. 15, no. 2, pp. 208-219, Dec. 2024.

revolute-revolute (PRRR) manipulator used in the robotic charging station (RoCharg-v1), as shown in Figure 1, including its counterweight mechanism and joint accuracy are available in [3][4]. These sources explore key design considerations, joint configurations, and precision control critical to optimal manipulator performance in alignment tasks.

Most current force sensors, especially in end-effectors, are rigid and struggle to handle dynamic, multi-directional forces [5], leading to misalignment and potential damage in systems like EV charging ports. Advances in flexible materials and sensor technology have significantly enhanced adaptability in dynamic environments, particularly in areas such as human-machine interfaces and soft robotics [6]. Flexible sensors play a crucial role in improving a robot's perception and its ability to adapt to its surroundings by accurately estimating mechanical stimuli and deformation [7]. However, accurately measuring three-axis forces in complex systems, such as EV charging ports, remains a challenge. These systems require a combination of precision and flexibility to achieve optimal performance and reliability.

Research on remote center compliance (RCC) in EV charging ports focuses on improving automated system efficiency and reliability. Recent advancements include adaptive compliance control with fuzzy impedance rules, and enhancing manipulator performance by reducing tracking errors and insertion

times [8]. A compliant plugging strategy with force feedback and admittance control addresses pose deviations, using a search algorithm to mitigate visual positioning errors [9]. Additionally, mobile EV charging stations (MEVCS) improve accessibility by offering flexible, location-independent recharging options [10].

Recent advancements in three-axis force measurement technologies have led to the development of more accurate and versatile sensors across various fields, including robotics, sports science, and medical diagnostics [11][12][13]. Flexible three-axis sensors integrated into footwear utilize deep learning for gait analysis [14]. Tri-axis force refactoring enhances robotic accuracy by centralizing measurements [15], while capacitive and inductive sensors improve precision in robotics and biomechanics [16][17]. Furthermore, research employing long short-term memory (LSTM) models to estimate forces in the hand and wrist based on integrated electromyography (iEMG) signals demonstrates significant potential for performance analysis [18]. However, challenges related to calibration and data processing persist. Similarly, RCC devices have advanced force measurement in robotic assembly through the use of six-axis sensors and passive RCC systems, although optimization remains an ongoing challenge [19][20][21].

Three-axis force sensors based on magnetic fields have made significant advancements. Various methods

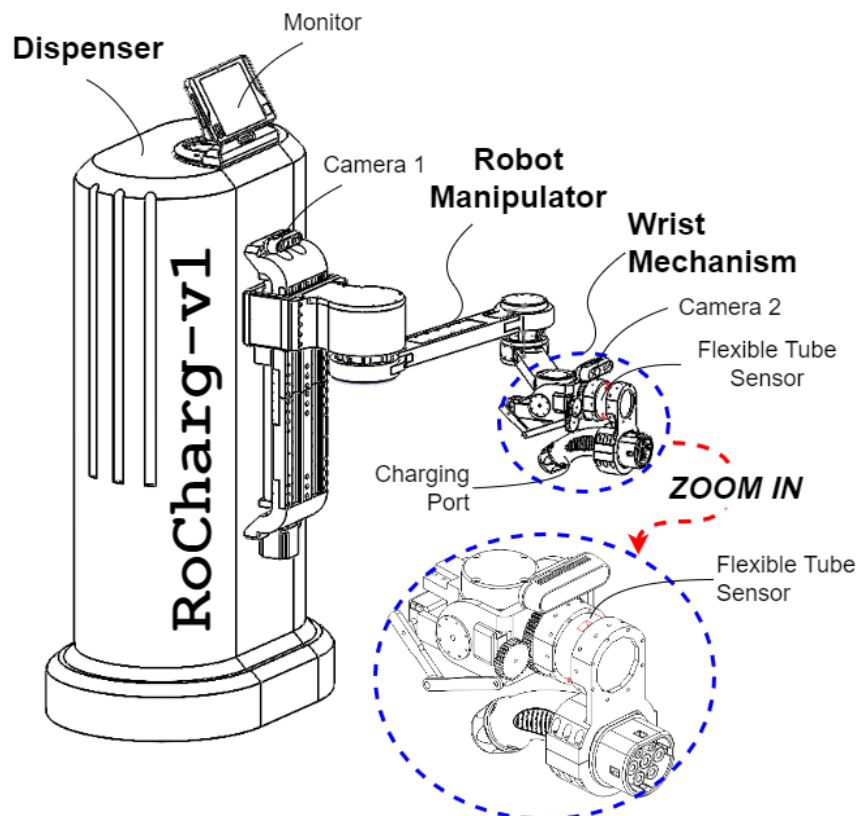


Figure 1. Implementing a flexible tube sensor for alignment in robotic charging.

have been employed to map the relationship between magnetic fields and forces, utilizing both conventional approaches and machine learning techniques [22][23][24]. One method developed a three-dimensional (3-D) magnetic soft force sensor with a mean absolute error (MAE) of 11.7 mN and a mean squared error (MSE) of less than  $1.16 \times 10^{-4}$ , with a force range of up to 1.5 N [25]. Another sensor achieved a maximum operating force of 5 N, with a relative deviation between 10 % and 35 %, and demonstrated better performance under moderate loading rates, achieving an MAE of 0.175 for training data and 0.201 for testing data, though it underperformed at high force levels and steep loading rates [26]. A magnetic tactile sensor exhibited high sensitivity for normal forces (16 mV/N), shear forces (30 mV/N), and angular forces (81 mV/N), with minimal crosstalk, good repeatability (maximum error of 6.4 %), low hysteresis (8.4 %), and force ranges of 0 N to 20 N (normal), 0 N to 3.5 N (shear), and 0 N to 1.5 N (angular) [27]. Furthermore, a Hall-effect-based multi-axis sensor demonstrated high sensitivity, with a force range as low as 0.2 N and minimal crosstalk between axes [28]. These innovations are crucial for improving force measurement accuracy in applications such as EV charging and robotics.

This paper introduces a novel three-axis flexible tube sensor fabricated from 3-D-printed thermoplastic polyurethane (TPU) for its flexibility and durability. The sensor integrates magnetic Hall-effect sensors to detect force variations along the  $x$ ,  $y$ , and  $z$  axes. LSTM networks are employed to enhance measurement accuracy, process time-series data, and adapt to real-time force changes [29]. This design makes the sensor ideal for dynamic environments like EV charging ports, improving alignment accuracy, reducing misalignment risks, and enhancing overall charging reliability.

The key contributions of this work are: First, the sensor's design and fabrication, using 3-D printing technology with TPU material, provides exceptional flexibility and resilience to mechanical stress. Second, the sensor's performance is validated through finite element method (FEM) analysis, which evaluates its deflection behavior under different loading conditions, ensuring its structural integrity. Third, magnetic Hall-effect sensors are employed to accurately measure three-axis forces applied to the charging port, enabling precise force measurements in the  $x$ ,  $y$ , and  $z$  directions. Lastly, an LSTM-based machine learning model is utilized to predict forces ( $F_x$ ,  $F_y$ ,  $F_z$ ) from sensor data ( $M_x$ ,  $M_y$ ,  $M_z$ ), significantly enhancing real-time adaptability and improving the accuracy of force measurements.

## II. Materials and Methods

### A. Flexible tube sensor design

In this study, the flexible tube sensor was designed to measure forces in 3-D ( $F_x$ ,  $F_y$ ,  $F_z$ ) while maintaining flexibility. TPU was selected for its mechanical properties, such as flexibility and resilience under stress. The tube, a hollow cylinder, was designed with key geometric parameters, including outer radius ( $r_o$ ), inner radius ( $r_i$ ), wall thickness ( $r_o - r_i$ ), and length ( $L$ ). These parameters ensured the tube could withstand multi-dimensional forces and perform under expected loading conditions. To analyze the tube's ability to resist bending deformations, the moment of inertia  $I$  of the tube's cross-section was calculated as equation (1) [30].

$$I = \frac{\pi}{4}(r_o^4 - r_i^4) \quad (1)$$

The bending deflection of the tube under applied forces ( $F$ ) was calculated using beam deflection theory. The maximum deflection  $\delta$  for a tube was determined using the equation (2).

$$\delta = \frac{FL^3}{3EI} \quad (2)$$

with an  $E$  is Young's modulus. To evaluate the axial stress in the tube under forces applied along its length, the axial stress  $\sigma_x$  was calculated using equation (3).

$$\sigma_x = \frac{F_x}{A} \quad (3)$$

where  $F_x$  is the axial force, and  $A$  is the cross-sectional area of the tube, given by

$$A = \pi(r_o^2 - r_i^2) \quad (4)$$

For a flexible tube, shear deformation can also be important, particularly if the tube is short relative to its diameter. The shear deflection ( $\delta_s$ ) can be given by

$$\delta_s = \frac{FL}{A_s G} \quad (5)$$

where  $A_s$  is the shear area of the tube, which can be approximated for thin-walled tubes as

$$A_s = 2\pi r_m t \quad (6)$$

where  $r_m$  is the mean radius,  $t$  is the wall thickness,  $G$  is the shear modulus of the TPU, and  $L$  is the length of the tube.

For torsional loading, the angle of twist  $\theta$  was calculated to assess the tube's resistance to twisting forces [30]. The angle of twist was determined using equation (7)

$$\theta = T \frac{L}{GJ} \quad (7)$$

$$J = \frac{\pi}{2}(r_o^4 - r_i^4) \quad (8)$$

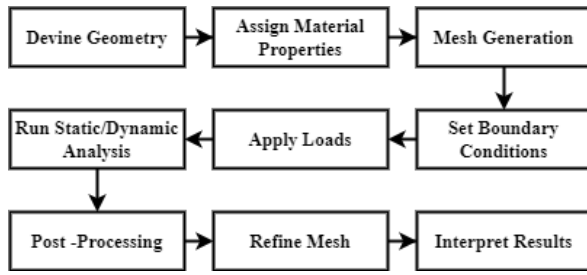


Figure 2. Block diagram for conducting FEM analysis for a flexible tube sensor.

where  $T$  is the applied torque and  $J$  is the polar moment of inertia. For cases where the tube was subjected to combined forces in the  $x$ ,  $y$ , and  $z$  directions, the total deflection  $\delta_{total}$  was calculated using the equation (9).

$$\delta_{total} = \sqrt{\delta_x^2 + \delta_y^2 + \delta_z^2} \quad (9)$$

where  $\delta_x$ ,  $\delta_y$ , and  $\delta_z$  are the deflections in the  $x$ ,  $y$ , and  $z$  directions, respectively. This provided a comprehensive understanding of the tube's deformation under multi-dimensional loading conditions, ensuring the design was robust enough to handle operational forces in practical applications.

### 1) Material and fabrication

The flexible tube sensor is fabricated using TPU, which was chosen for its flexibility, durability, and high resistance to fatigue and wear. TPU's elasticity, abrasion resistance, and ability to perform well in varied environments make it ideal for this application. Its Young's modulus ( $E$ ) (10 Mpa to 100 MPa) provides a balance between stiffness and flexibility, while a Poisson's ratio ( $\nu$ ) of 0.48 allows it to withstand deformation under tension. With a density ( $\rho$ ) of 1.1 g/cm<sup>3</sup> to 1.25 g/cm<sup>3</sup> and a shear modulus ( $G$ ) of 3 MPa to 40 MPa, TPU is lightweight yet strong. During 3-D printing, TPU filaments with a Shore hardness of 85A-98A are used at 220 °C to 250 °C, with a bed temperature of 40 °C to 60 °C, ensuring proper adhesion for applications like gaskets, protective cases, and flexible prototypes [31][32].

### 2) Magnetic sensor

The CJMCU-90393, a high-precision three-axis magnetic sensor, detects small variations in magnetic fields corresponding to forces along the  $x$ ,  $y$ , and  $z$  axes. It measures field strengths from 5 mT to 50 mT with a resolution of up to 0.161  $\mu$ T per least significant bit (LSB). With a sampling rate of 500 Hz and low power consumption (100  $\mu$ A active, 1  $\mu$ A to 2  $\mu$ A idle), it is ideal for compact, power-sensitive systems like robotic alignment and contactless sensing applications [33][34]. Embedded in the center of a flexible tube, the sensor

tracks field variations caused by deformations, enabling 3-D force measurement. FEM analysis is used for deflection of flexible tube sensor.

### 3) FEM analysis

In this study, FEM analysis was used to evaluate the behavior of a flexible tube sensor designed to measure forces in one-dimension (1-D) ( $F_y$ ). The tube, made from TPU, was modeled using key material properties: elastic modulus of 26 MPa, density of 1,225.49 kg/m<sup>3</sup>, and tensile strength of 39 MPa. The analysis employed the hyperelastic Blatz-Ko model to simulate the non-linear elastic response of the TPU under applied forces.

The governing elasticity equations used in the FEM analysis relate to stress, strain, and displacement through Hooke's law [35]. The relationship between the stress  $\sigma$  and strain  $\epsilon$  is expressed as

$$\sigma = E \cdot \epsilon \quad (10)$$

The strain-displacement relationship in 3-D was defined as equation (11).

$$\epsilon_{ij} = \frac{1}{2} \left( \frac{\partial u_i}{\partial u_j} + \frac{\partial u_j}{\partial u_i} \right) \quad (11)$$

where  $u_i$  represents the displacement components in the  $x$ ,  $y$ , and  $z$  directions. These equations are used to analyze the deformation of the tube when forces are applied in the  $x$ ,  $y$ , and  $z$  directions. The ends of the tube are constrained to prevent any movement, simulating fixed boundary conditions. Forces were applied to simulate the expected loading scenarios in the  $x$ ,  $y$ , and  $z$  directions, respectively.

The tube geometry was discretized into finite elements, using a fine mesh to ensure accuracy in high-stress regions. Post-processing included von Mises stress analysis to confirm the TPU material stayed within its elastic limits, and strain energy distribution was evaluated to observe deformation under various loads. This FEM analysis provided critical insights into the tube's ability to measure forces in 3-D and confirmed its structural integrity for real-world applications. The simulation process is shown in Figure 2.

## B. LSTM modeling

### 1) Input data and pre-processing

The input to the LSTM model consists of time-series data from Hall-effect sensors embedded in the flexible tube. The raw magnetic field data is pre-processed to normalize values, improving accuracy and training efficiency. Data is collected from a Flexible Tube Sensor mounted in parallel with an AFT200-D80-C force per torque (F/T) sensor (see Figure 3), capturing the relationship between magnetic field

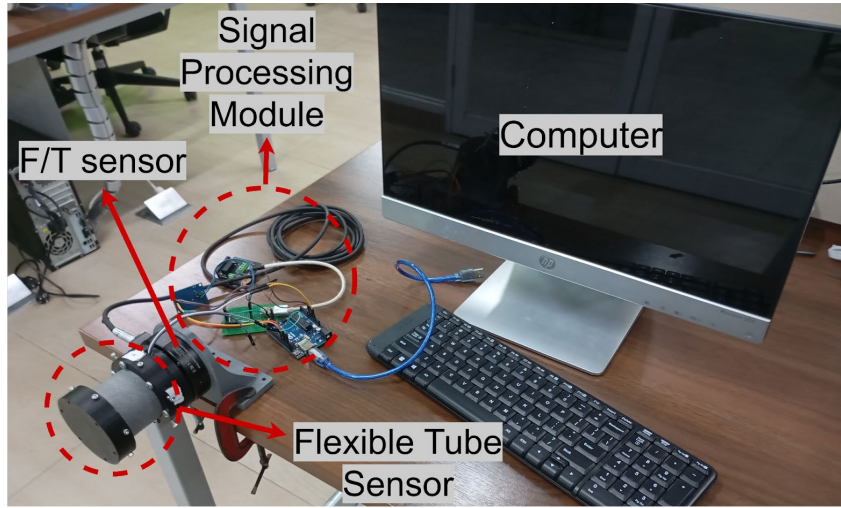


Figure 3. Installation of a flexible tube sensor paralleled with an F/T sensor is for data set creation and validation purposes.

variations and force. A moving average filter is applied to reduce noise, enhancing the dataset for accurate force prediction by the LSTM model.

Before model training, the data undergoes pre-processing. Any damaged or not a number (NaN)-containing datasets are inspected and filled with the mean values. Normalization is also performed to ensure that all features are on the same scale using standardization. This process is crucial for the model as a well-prepared dataset enhances the quality of the trained model. Next, the data is split into training and testing sets with an 80 % to 20 % ratio, ensuring that the model is tested on data it has not previously encountered.

## 2) LSTM network architecture

The LSTM model is structured with an input layer, one or more hidden LSTM layers, and an output layer. The core LSTM operations are defined by equation (12) to equation (21) [36], which control how the model processes the magnetic field input to predict forces.

### a) Forget gate

Determines what information from the previous time step's cell state  $C_{t-1}$  should be discarded:

$$f_t = \sigma(W_f \cdot [h_{t-1}, x_t] + b_f) \quad (12)$$

$$x_t = [M_x, M_y, M_z] \quad (13)$$

where  $f_t$  is forget gate,  $W_f$  is the weight of the forget gate,  $x_t$  represents the magnetic field input at time  $t$ ,  $b_f$  is bias of the forget gate.

### b) Input gate

Determines what new information will be added to the cell state:

$$i_t = \sigma(W_i \cdot [h_{t-1}, x_t] + b_i) \quad (14)$$

$$\hat{C}_t = \tanh(W_c \cdot [h_{t-1}, x_t] + b_c) \quad (15)$$

where  $i_t$  is input gate,  $W_i$  and  $W_c$  are weights,  $b_i$  and  $b_c$  are biases. The input gate controls the flow of new information into the memory cell, while the candidate cell state  $\hat{C}_t$  captures the influence of the magnetic field data.

### c) Cell state update

The new cell state  $C_t$  is updated based on the input and forget gates:

$$C_t = f_t \cdot C_{t-1} + i_t \cdot \hat{C}_t \quad (16)$$

### d) Output gate

Controls the output of the cell state to the next hidden state:

$$o_t = \sigma(W_o \cdot [h_{t-1}, x_t] + b_o) \quad (17)$$

$$h_t = o_t \cdot \tanh C_t \quad (18)$$

where  $o_t$  is output gate,  $W_o$  and  $b_o$  are the weight and bias for the output gate. The hidden state  $h_t$  is then passed to the output layer to generate the predicted forces.

## 3) Force prediction

After processing the magnetic field data through the LSTM network, the output layer predicts the corresponding forces ( $F_x, F_y, F_z$ ) at each time step, given by:

$$\hat{F}_t = W_{out} \cdot h_t + b_{out} \quad (19)$$

$$\hat{F}_t = [\hat{F}_x, \hat{F}_y, \hat{F}_z] \quad (20)$$

where  $\hat{F}_t$  represents the predicted forces,  $W_{out}$  is the weight matrix for the output layer,  $b_{out}$  is the bias for the output layer.

## 4) Training the LSTM model

The LSTM model is trained using a dataset that includes various force measurement conditions to

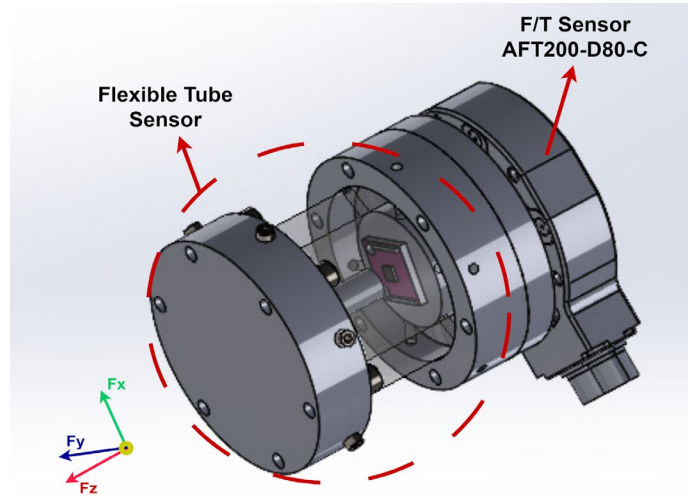


Figure 4. Design of a Flexible tube sensor in parallel with a F/T sensor and its coordinate axes.

ensure robustness. The dataset maps magnetic field inputs ( $M_x$ ,  $M_y$ ,  $M_z$ ) to corresponding force measurements ( $F_x$ ,  $F_y$ ,  $F_z$ ). By learning from past data points, the LSTM model improves accuracy in predicting forces from real-time sensor readings. The model focuses on time-series data, capturing the relationship between magnetic field variations and force outputs. The training minimizes the MSE between predicted and actual forces to enhance prediction accuracy [37].

$$\text{MSE} = \frac{1}{n} \sum_{t=1}^n \left( (F_{x,t} - \hat{F}_{x,t})^2 + (F_{y,t} - \hat{F}_{y,t})^2 + (F_{z,t} - \hat{F}_{z,t})^2 \right) \quad (21)$$

where  $n$  is the number of time steps;  $F_{x,t}$ ,  $F_{y,t}$ ,  $F_{z,t}$  are the actual forces;  $\hat{F}_{x,t}$ ,  $\hat{F}_{y,t}$ ,  $\hat{F}_{z,t}$  are the predicted forces. The model is trained using gradient descent, adjusting the weights and biases to minimize the loss function.

##### 5) Model performance evaluation

The LSTM model's performance is evaluated by comparing predicted forces with actual measurements using MSE and the coefficient of determination ( $R^2$ ). MSE quantifies the average difference between predictions and actual values, while  $R^2$  indicates the proportion of variance explained by the model. To assess adaptability in dynamic conditions like EV charging ports, 20% of the dataset is reserved for validation. This evaluates the model's accuracy in real-time applications such as robotic alignment and informs further optimization for improved precision.

### III. Results and Discussions

This section presents the results and analysis of the proposed three-axis flexible tube sensor. FEM analysis highlights the sensor's deflection behavior under various loads, with the tube design shown in Figure 4.

The sensor's real-time performance is evaluated, focusing on the effectiveness of the LSTM model in predicting forces in dynamic environments. The discussion compares the sensor with existing technologies, demonstrating how it addresses limitations in flexibility and precision for multi-axis force measurement, particularly in EV charging port applications.

#### A. FEM analysis results

The simulation was conducted to determine the stress and displacement of the sensor when subjected to a load. Figure 5 shows the displacement of the sensor under a load of 30 N maximum. According to the simulation, the deformation of the sensor reaches 3.16 cm at the front, indicated by the red color in Figure 5(a). This significant displacement is largely due to the elastic properties of the TPU material used in the sensor.

Figure 5(b) presents two graphs that depict the relationship between stress and force as well as displacement and force. Both graphs exhibit a linear relationship. In the stress vs force plot, the stress steadily increases with the applied force, demonstrating that the material operates within its elastic region for forces ranging from 0 N to 30 N. The stress reaches approximately  $1.5 \times 10^5$  N/m<sup>2</sup> at 30 N, indicating that the material adheres to Hooke's law, maintaining proportionality between stress and applied force [35]. Similarly, the displacement vs force graph reveals a linear increase in displacement, which reaches 3 cm at the maximum applied force of 30 N. This consistent linearity suggests uniform deformation of the material without exceeding its elastic limit. Both graphs confirm that the flexible tube sensor is functioning as intended, with predictable elastic behavior and structural integrity maintained across the tested force range.

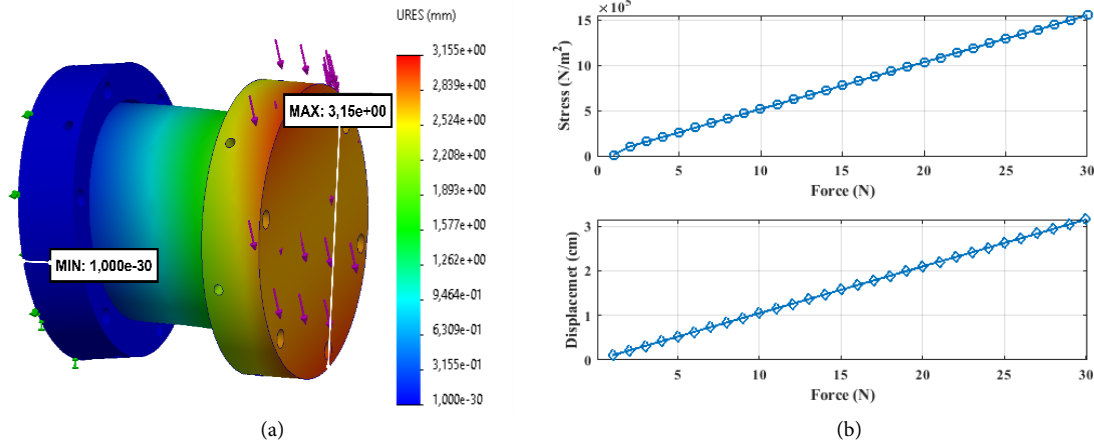


Figure 5. Finite element analysis (FEA) of the flexible tube sensor assembly under a force in the Y-axis: (a) deformation with displacement magnitude contours; (b) stress and displacement.

## B. LSTM model performance

The training results indicate that the LSTM model has successfully mapped the relationship between the magnetic field and force for each axis ( $F_x$ ,  $F_y$ ,  $F_z$ ). The system employs sequential data processing with a timestep of 10. The use of StandardScaler improved the model's performance by normalizing the data to maintain a consistent scale. The dataset used in this study consists of 17,293 rows. Utilizing the train-test split technique, 20 % of the dataset (3,458 rows) was allocated for validation to ensure an objective evaluation of the model's generalization capability [38].

In Figure 6, the loss graph shows a consistent decrease for both training and validation losses, stabilizing around 60 epochs. This indicates that the model has optimally identified patterns in the data without overfitting, as evidenced by the minimal difference between the training and validation losses. Additionally, the graph shows that training stopped at 146 epochs, indicating the activation of early stopping due to no improvement in validation loss for 10 consecutive epochs.

Figure 6 also demonstrates that the LSTM model performed effectively and reliably during the training process. The graph indicates that the model successfully achieved convergence, with training and validation loss values approaching zero. This is attributed to the model's ability to capture data patterns with high accuracy. The minimal difference between training and validation losses further reflects effective regularization, enabling the model to generalize well when tested on previously unseen data.

Figure 7 illustrates the comparison between the actual and predicted force values along the  $x$ ,  $y$ , and  $z$  axes based on the training results. The three graphs in Figure 7 represent the testing results of 250 samples, derived from 20 % of the dataset used for model validation. In Figure 7(a), the actual force ( $F_x$ ) ranges between approximately -10 N to 10 N, while the predicted values generally follow this range, though there are some deviations where the predicted values are higher or lower. For instance, at sample index 2,800, the predicted value undershoots to around 5 N, while the actual value is closer to 7 N. In Figure 7(b), for the

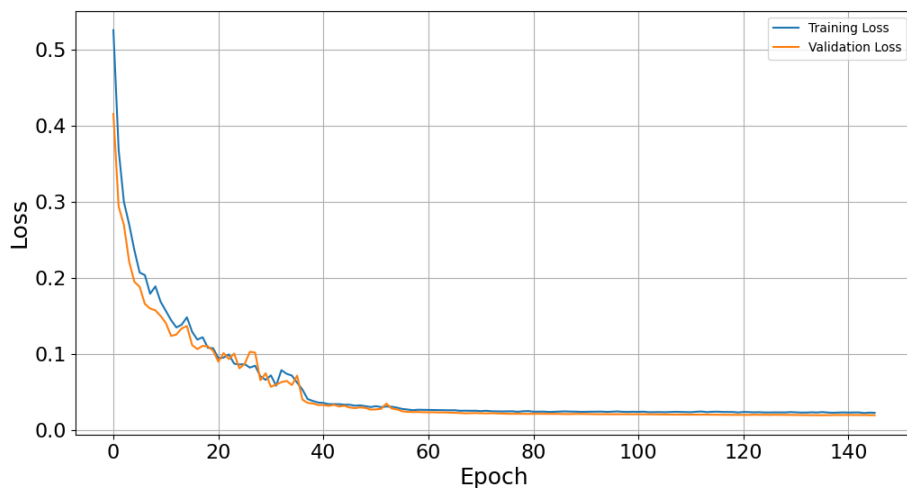
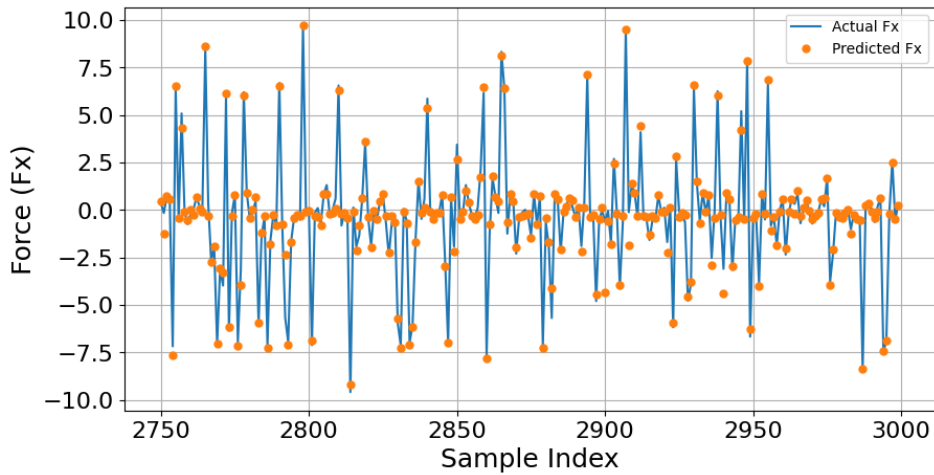


Figure 6. Training loss vs validation loss during model training.

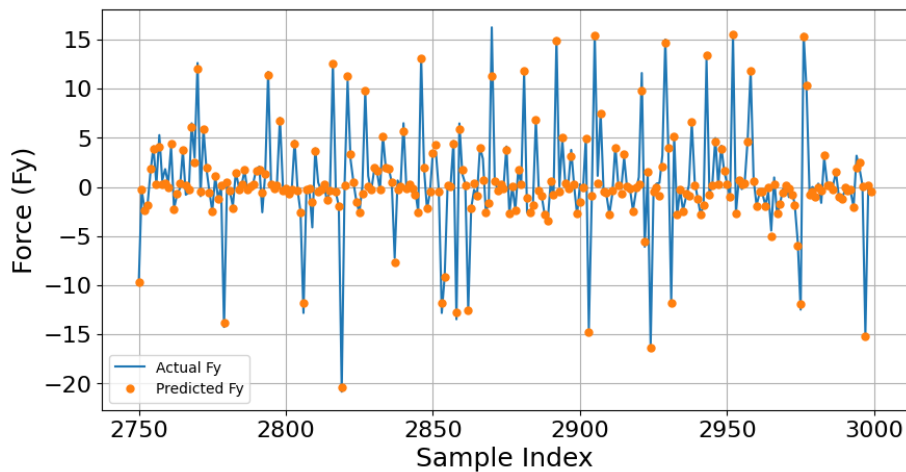
$y$ -axis ( $F_y$ ), the actual force fluctuates between -20 N and 15 N, and the predicted values follow the overall trend but tend to smooth out sharper variations, especially between indices 2,850 to 2,900. Lastly, in Figure 7(c), the actual force on the  $z$ -axis ( $F_z$ ) varies between -30 N and 40 N, with predicted values closely following the general pattern but sometimes failing to capture peak variations, such as at sample index 2,950,

where the actual force spikes to around 40 N, but the predicted force remains lower at about 35 N. These discrepancies indicate that while the model tracks general trends, it struggles to capture rapid force changes, particularly at higher magnitudes fully.

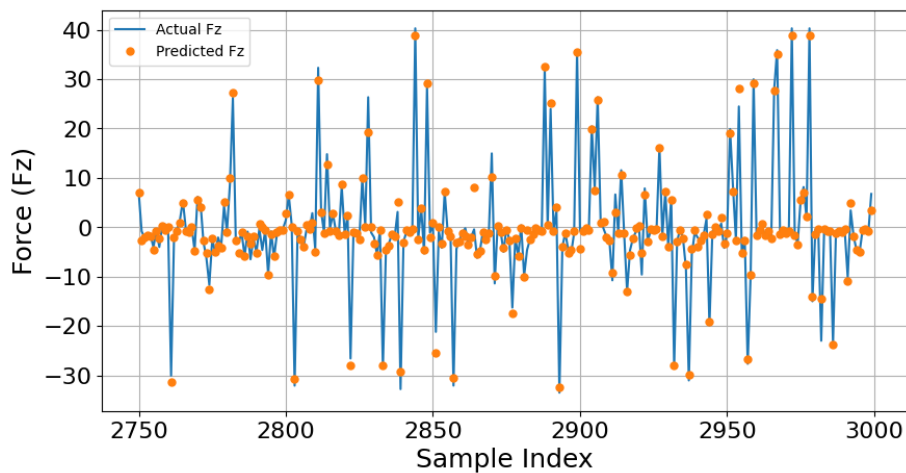
The model evaluation using MSE and  $R^2$  score confirms that the training produced a well-performing model, as illustrated in Figure 7(a) to Figure 7(c). For



(a)



(b)



(c)

Figure 7. Comparison between actual and predicted force values on the three axes within a certain range during training: (a) performance on the  $x$ -axis; (b) performance on the  $y$ -axis; (c) performance on the  $z$ -axis.



the  $F_x$  axis, the model achieved an MSE of 0.1132 and an  $R^2$  score of 0.9886. On the  $F_y$  axis, the MSE was 0.4166, with an  $R^2$  score of 0.9819. For the  $F_z$  axis, the MSE was 1.6058, and the  $R^2$  score reached 0.9856. Overall, the model can be considered effective, given that all  $R^2$  scores exceed 0.98 and the MSE values are relatively low, suggesting an absence of overfitting in the model. However, the MSE for the  $F_z$  axis is

significantly higher than the other axes, which may be attributed to greater variation or a wider range in the  $F_z$  data compared to the  $F_x$  and  $F_y$  axis.

The trained LSTM model was subsequently tested using new data with the same format as the dataset used during training. The test data consists of 2,000 rows that were not included in the model training process. Figure 8 presents a section of the graph showing the

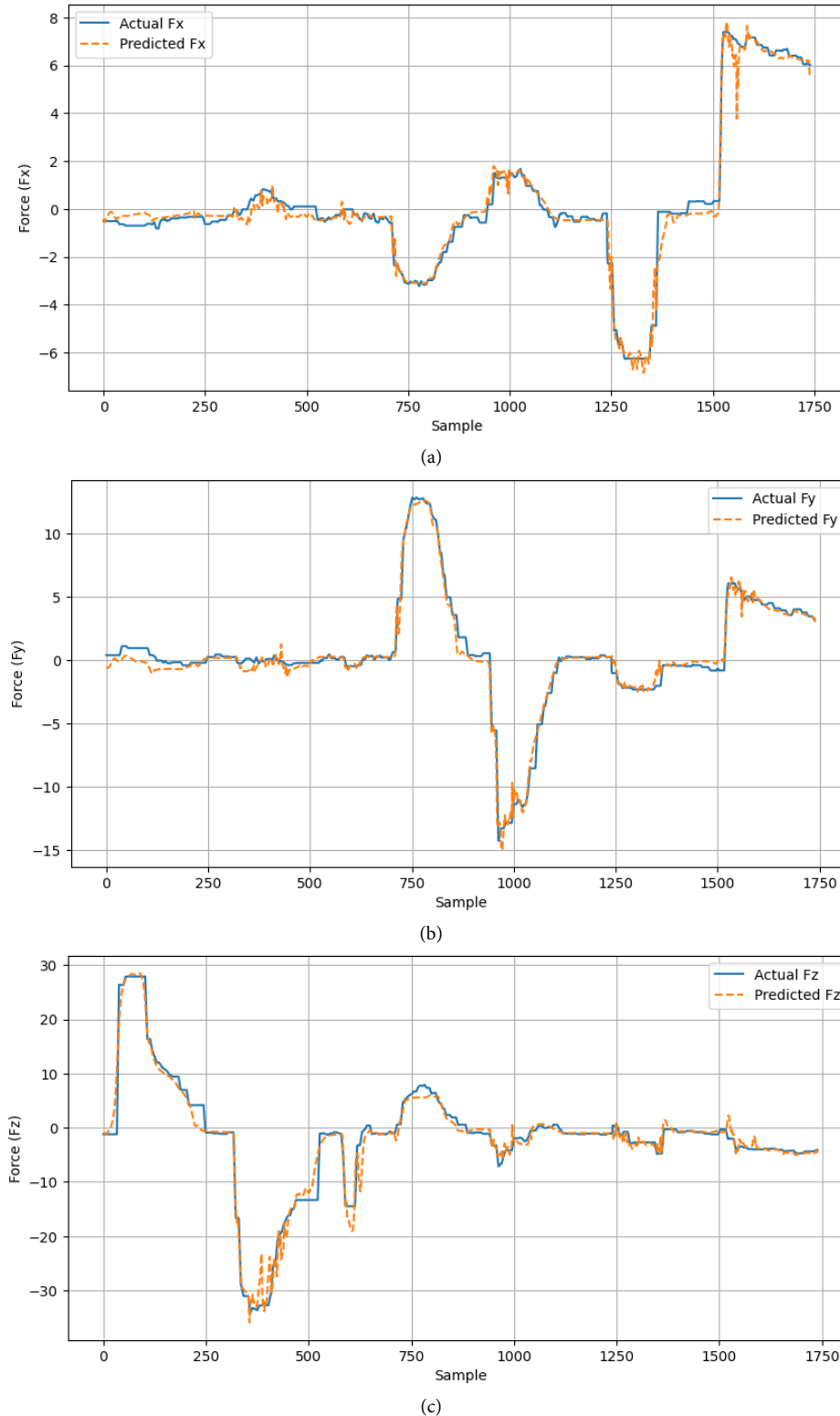


Figure 8. Testing results depicting force measurements along the three axes: (a) force on the  $x$ -axis; (b) force on the  $y$ -axis; (c) force on the  $z$ -axis.

LSTM model testing results. Figure 8(a) presents the testing results of the model for the  $F_x$  axis. It can be observed that the model predicts the force quite accurately, and the predicted values (dashed orange line) closely follow the actual data (blue line). The deviation between the predicted and actual values appears to be evenly distributed across the graph with relatively small magnitudes. Figure 8(b) presents the testing results for the  $F_y$  axis, where the prediction pattern closely resembles the actual data pattern. However, slight deviations are observed around points of drastic changes. Figure 8(c) presents the testing results for the  $F_z$  axis. The force prediction on the  $F_z$  axis demonstrates a predictive pattern that remains aligned with the actual pattern; however, several significant deviations can be observed at certain points, particularly in areas experiencing substantial changes in force. These large deviations are likely due to the much wider range of force values compared to the  $F_x$  and  $F_y$  axes.

The testing results were also evaluated using MSE and  $R^2$  scores. The MSE value for the  $F_x$  axis is 0.2819, with an  $R^2$  score of 0.9722, indicating excellent predictive performance for the force along the  $x$ -axis. The  $F_y$  axis has an MSE of 0.3567 and an  $R^2$  score of 0.9795. While the MSE for the  $F_y$  axis is slightly higher than that for the  $F_x$  axis, it achieves a better  $R^2$  score than  $F_x$ . Lastly, for the  $F_z$  axis, the model yielded an MSE of 2.8086 and an  $R^2$  score of 0.9713. The MSE for the  $F_z$  axis is significantly higher compared to  $F_x$  and  $F_y$ , suggesting that the model faces some challenges in predicting forces along the  $F_z$  axis.

The LSTM model demonstrates exceptional performance in predicting forces based on variations in magnetic field values, as evidenced by relatively low MSE values and  $R^2$  scores exceeding 97% across all three axes, with a force measurement range of up to 30 N for each axis. The small and evenly distributed deviations observed in the graphs for the  $F_x$  and  $F_y$  axes highlight the model's strong generalization capabilities, high consistency, minimal random errors, and outstanding accuracy.

## IV. Conclusion

This research presents a novel approach for predicting multi-axis forces in a flexible tube sensor by combining Hall-effect sensors with an LSTM network. The sensor, fabricated from TPU, demonstrated high flexibility and resilience, allowing accurate measurement of forces in the  $x$ ,  $y$ , and  $z$  directions. The LSTM model achieved strong performance, with MSE values of 0.2819 ( $F_x$ ), 0.3567 ( $F_y$ ), and 2.8086 ( $F_z$ ), and  $R^2$  scores exceeding 0.97 on all axes. FEM analysis

further validated the sensor's capability, showing that it can withstand forces up to 30 N without exceeding the elastic limit, with a maximum stress of  $1.5 \times 10^5$  N/m<sup>2</sup> and a displacement of 3 cm. Despite the relatively higher MSE on the  $F_z$  axis due to larger variations, the overall reliability of the model remains uncompromised. The findings are significant as they address challenges in improving the precision and reliability of automated EV charging port alignment systems. By reducing misalignment risks and enhancing operational robustness, this sensor design contributes to more efficient and reliable charging processes. Furthermore, this research lays a strong foundation for the advancement of hybrid models, particularly by integrating LSTM with support vector machine (SVM) to enhance force prediction accuracy. In addition to its current application in EV charging systems, the sensor design holds significant potential for broader use in dynamic environments. These include robotic assembly and soft robotics, where precise multi-axis force measurements are essential for ensuring reliability and efficiency in operations.

## Acknowledgements

The authors wish to thank the Research Center for Smart Mechatronics – National Research and Innovation Agency (BRIN) for their financial support through the "Rumah Program." This research, part of the project titled "Wrist Mechanism for Manipulator of Automatic Charging Station", was funded under letter Number 2/III.6/HK/2024.

## Declarations

### Author contribution

All authors contributed equally as the main contributor of this paper. All authors read and approved the final paper.

### Funding statement

This work was conducted as part of the collaborative research grant between University of Technology Malaysia (UTM) and BRIN, with grant number R.J130000.7351.4B734.

### Competing interest

The authors declare that they have no known competing financial interests or personal relationships that could have appeared to influence the work reported in this paper.

## Additional information

**Reprints and permission:** information is available at <https://mev.brin.go.id/>.

**Publisher's Note:** National Research and Innovation Agency (BRIN) remains neutral with regard to jurisdictional claims in published maps and institutional affiliations.

## References

- [1] H. M. Saputra et al., "Characterization of plugging and unplugging process for electric vehicle charging connectors based on Force/Torque measurements," *Measurement*, vol. 242, p. 115876, 2025.
- [2] H. M. Saputra, N. S. M. Nor, E. Rijanto, M. Z. Md Zain, I. Z. Mat Darus, and E. Yazid, "A review of robotic charging for electric vehicles," *Int J Intell Robot Appl*, vol. 8, no. 1, 2024.
- [3] H. M. Saputra, B. Abdussalam, C. H. A. H. B. Baskoro, N. S. M. Nor, T. Permadi, and M. Y. Rezaldi, "Counterweight mechanism of prismatic joint at 4-DOF PRRR manipulator for robotic charging station (RoCharg-v1)," in *Proceedings - 2023 10th International Conference on Computer, Control, Informatics and its Applications: Exploring the Power of Data: Leveraging Information to Drive Digital Innovation, IC3INA 2023*, 2023.
- [4] H. M. Saputra, T. Permadi, C. H. A. H. B. Baskoro, N. S. M. Nor, B. Abdussalam, and M. Y. Rezaldi, "Effect of IMU sensor positioning on 1-DOF angle measurement accuracy for robotic charging station (RoCharg-v1) Manipulator," in *Proceedings - 2023 10th International Conference on Computer, Control, Informatics and its Applications: Exploring the Power of Data: Leveraging Information to Drive Digital Innovation, IC3INA 2023*, 2023.
- [5] S. Pyo, J. Lee, K. Bae, S. Sim, and J. Kim, "Recent progress in flexible tactile sensors for human-interactive systems: from sensors to advanced applications," *Advanced Materials*, 33(47): e2005902, April, 2021.
- [6] E. Liu, Z. Cai, Y. Ye, M. Zhou, H. Liao, and Y. Yi, "An overview of flexible sensors: Development, application, and challenges," *Sensors*, 23, 817, 2023.
- [7] D. Kim et al., "Review of machine learning methods in soft robotics," *PLoS One*, vol. 16, no. 2 February, 2021.
- [8] J. Huang et al., "Fuzzy adaptive compliance control method for charging manipulator," in *2023 IEEE International Conference on Mechatronics and Automation, ICMA 2023*, 2023.
- [9] W. He and R. Li, "Research on compliant plugging strategy for electric vehicle charging port based on force feedback," in *ACM International Conference Proceeding Series*, 2022.
- [10] R. Gopalakrishnan, D. S. Vidhya, R. Gowshickraaj, E. Kamalakannan, and S. Narendran, "Design and implementation of roving charging station for electric vehicles," in *7th International Conference on Trends in Electronics and Informatics, ICOEI 2023 - Proceedings*, 2023.
- [11] S. Li and J. Xu, "Multi-axis force/torque sensor technologies: design principles and robotic force control applications: A review," *IEEE Sens J*, vol. PP, p. 1, Jan. 2024.
- [12] A. Alotaibi, "Flexible 3D force sensor based on polymer nanocomposite for soft robotics and medical applications," *Sensors*, vol. 24, no. 6, 2024.
- [13] S. Park and D. Hwang, "Three-axis flat and lightweight force/torque sensor for enhancing kinesthetic sensing capability of robotic hand," *IEEE Transactions on Industrial Electronics*, vol. 71, no. 10, 2024.
- [14] Q. Zhang et al., "A wearable three-axis force sensor based on deep learning technology for plantar measurement," *Chemical Engineering Journal*, vol. 482, 2024.
- [15] J. Jin, S. Wang, D. Mei, C. Mao, and Y. Wang, "A novel flexible centralized force sensor based on tri-axis force refactoring method for arbitrary force components measurement," *Advanced Intelligent Systems*, vol. 6, no. 1, 2024.
- [16] J. Fernandes, J. Chen, and H. Jiang, "Three-axis capacitive sensor arrays for local and global shear force detection," *Journal of Microelectromechanical Systems*, vol. 30, no. 5, 2021.
- [17] R. Moscoso, R. Callupe, J. Garcia, and E. R. Villota, "Three-axis sensor development for ground reaction forces measurement with sports applications," in *Smart Innovation, Systems and Technologies*, 2022.
- [18] A. E. Olsson, N. Malešević, A. Björkman, and C. Antfolk, "End-to-end estimation of hand- and wrist forces from raw intramuscular EMG signals using LSTM Networks," *Front Neurosci*, vol. 15, 2021.
- [19] U. Kim et al., "Displacement Sensor Integrated into a Remote Center Compliance Device for a Robotic Assembly," *IEEE Access*, vol. 9, 2021.
- [20] L. J. Lai and Z. N. Zhu, "Modeling and analysis of a compliance model and rotational precision for a class of remote center compliance mechanisms," *Applied Sciences (Switzerland)*, vol. 6, no. 12, 2016.
- [21] J. Park, H. S. Kim, D. Il Park, and C. H. Park, "Smart passive compliance device system for precision assembly task with industrial robot," in *2018 15th International Conference on Ubiquitous Robots, UR 2018*, 2018.
- [22] D. S. Chathuranga, Z. Wang, Y. Noh, T. Nanayakkara, and S. Hirai, "A soft three axis force sensor useful for robot grippers," in *IEEE International Conference on Intelligent Robots and Systems*, 2016.
- [23] Z.-X. Dai and M.-H. You, "Modeling and measurement of CMOS-based three-axis magnetic field sensors with low cross-sensitivity," *IEEE Sens J*, vol. PP, p. 1, Nov. 2024.
- [24] H. Wang et al., "Design methodology for magnetic field-based soft tri-axis tactile sensors," *Sensors (Switzerland)*, vol. 16, no. 9, 2016.
- [25] A. Dwivedi, A. Ramakrishnan, A. Reddy, K. Patel, S. Ozel, and C. D. Onal, "Design, modeling, and validation of a soft magnetic 3-d force sensor," *IEEE Sens J*, vol. 18, no. 9, 2018.

- [26] M. Rabbani, M. Amin Mirzaee, M. Robati, and A. Sadighi, "Design and fabrication of a soft magnetic tactile sensor," in *10<sup>th</sup> RSI International Conference on Robotics and Mechatronics, ICRoM 2022*, 2022.
- [27] M. Rehan, M. M. Saleem, M. I. Tiwana, R. I. Shakoor, and R. Cheung, "A soft multi - axis high force range magnetic tactile sensor for force feedback in robotic surgical systems," *Sensors*, vol. 22, no. 9, 2022.
- [28] S. D. Moosavi Nasab, A. Beiranvand, M. Tale Masouleh, F. Bahrami, and A. Kalhor, "Design and development of a multi-axis force sensor based on the hall effect with decouple structure," *Mechatronics*, vol. 84, 2022.
- [29] J. Xin, T. Xu, J. Zhu, H. Wang, and J. Peng, "Long short - term memory - based multi - robot trajectory planning: learn from MPCC and make it better," *Advanced Intelligent Systems*, vol. 6, Jul. 2024.
- [30] F. P. Beer, E. R. Johnston, J. T. DeWolf, D. F. Mazurek, and S. Sanghi, *Mechanics of Materials*. McGraw-Hill Education (India) Private Limited, 2017.
- [31] M. Dwamena, "How to 3D print TPU filament like a pro - ultimate guide & FAQ," 3dprinterly. [Online] [Accessed: Dec. 13, 2024]
- [32] Martin, "3D printing with TPU - properties, tips & best settings," The 3D Printer Bee. [Online] [Accessed: Dec. 13, 2024]
- [33] K. Townsend, "MLX90393 wide-range 3-Axis Magnetometer." [Online] [Accessed: Dec. 13, 2024]
- [34] "Datasheet for MLX90393," Malexis. [Online] [Accessed: Dec. 13, 2024]
- [35] T. Böhlke and C. Brüggemann, "Graphical representation of the generalized Hooke's law," *Technische Mechanik*, vol. 21, Jan. 2001.
- [36] Y. Yu, X. Si, C. Hu, and J. Zhang, "A review of recurrent Neural Networks: LSTM cells and network architectures," *Neural Comput.*, 31(7): 1235-1270, 2019.
- [37] D. Chicco, M. J. Warrens, and G. Jurman, "The coefficient of determination R-squared is more informative than SMAPE, MAE, MAPE, MSE and RMSE in regression analysis evaluation," *PeerJ Comput Sci*, vol. 7, p. e623, 2021.
- [38] V. R. Joseph, "Optimal ratio for data splitting," *Statistical Analysis and Data Mining: The ASA Data Science Journal*, vol. 15, no. 4, pp. 531-538, Aug. 2022.